# Superionic iron oxide-hydroxide in Earth's deep mantle

**Authors:** Mingqiang Hou[1,2,*], Yu He[3,1,*], Bo Gyu Jang[1,4], Shichuan Sun[3], Yukai Zhuang[1], Liwei Deng[5], Ruilian Tang[1,6], Jiuhua Chen[7], Feng Ke[8], Yue Meng[9], Vitali B. Prakapenka[10], Bin Chen[1], Ji Hoon Shim[4], Jin Liu[1], Duck Young Kim[1], Qingyang Hu[1], Chris J. Pickard[11,12], Richard J. Needs[13], and Ho-Kwang Mao[1]

**Affiliations:**

[1]Center for High Pressure Science and Technology Advanced Research (HPSTAR), Beijing 100094, China

[2]Institute of Meteoritics, Department of Earth and Planetary Sciences, University of New Mexico, Albuquerque, NM 87131, USA

[3]Key Laboratory of High-Temperature and High-Pressure Study of the Earth's Interior, Institute of Geochemistry, Chinese Academy of Sciences, Guiyang, Guizhou 550081, China

[4]Department of Chemistry, Pohang University of Science and Technology, Pohang 37673, Korea

[5]College of New Materials and New Energies, Shenzhen Technology University, Guangdong 518118, China

[6]School of Materials Science and Engineering, Changchun University of Science and Technology, Changchun, 130022, China

[7]Center for Study of Matter under Extreme Conditions, Department of Mechanical and Materials Engineering, Florida International University, Miami, FL 33199, USA

[8]Department of Geological Sciences, Stanford University, Stanford, California 94305, USA

[9]Hight Pressure Collaborative Access Team, X-ray Science Division, Argonne National Laboratory, Argonne, Illinois 60439, USA

[10]Center for Advanced Radiation Sources, University of Chicago, Chicago, IL 60439, USA.

[11]Department of Materials Science and Metallurgy, University of Cambridge, 27 Charles Babbage Road, Cambridge CB3 0FS, United Kingdom

[12]Advanced Institute for Materials Research, Tohoku University, 2-1-1 Katahira, Aoba, Sendai, 980-8577, Sendai, Japan

[13]Theory of Condensed Matter Group, Cavendish Laboratory, JJ Thomson Avenue, Cambridge CB3 0HE, United Kingdom

*These authors contributed equally to this work.

**$H_2O$ ice becomes a superionic phase under the high pressure and temperature conditions of deep planetary interiors of ice planets such as Neptune and Uranus, which affects interior structures and generates magnetic fields. The solid Earth, however, contains only hydrous minerals with negligible amount of ice. Here we combine high pressure and temperature electrical conductivity experiments, Raman spectroscopy, and first-principles simulations, to investigate the state of hydrogen in the pyrite type $FeO_2H_x$ ($x \leq 1$) which is a potential H-bearing phase near the core-mantle boundary. We find that when the pressure increases beyond 73 GPa at room temperature, symmetric hydroxyl bonds are softened and the $H^+$ (or proton) become diffusive within the vicinity of its crystallographic site. Increasing temperature under pressure, the diffusivity of hydrogen is extended beyond individual unit cell to cover the entire solid, and the electrical conductivity soars, indicating a transition to the superionic state which is characterized by freely-moving proton and solid $FeO_2$ lattice. The highly diffusive hydrogen provides fresh transport mechanisms for charge and mass, which dictate the geophysical behaviors of electrical conductivity and magnetism, as well as geochemical processes of redox, hydrogen circulation, and hydrogen isotopic mixing in Earth's deep mantle.**

Hydrogen plays an important role in the deep interior of the Earth[1,2], where its mobility and bonding properties are altered dramatically from localized to globally itinerant with increasing depth. At shallower depths, hydrogen bonds with oxygen, the most abundant element in Earth, to form hydroxyls which modulate the electrical[3,4], thermal[5], and elastic[6] properties of the host minerals, and dictate redox, melting, and isotope partitioning[7]. Properties of hydroxyl groups have been extensively studied during the past half century as a means to locate deep water reservoirs and to monitor water circulation for a

broad range of applications in interpretation of large geophysical and geochemical features in depth[8-10]. Hydroxyl starts with an asymmetric configuration O-H···O in which the hydrogen atom between two oxygen atoms is bonded to one oxygen atom by a strong, short covalent bond (O-H) and to the other oxygen atom on the opposite side by a weak, long hydrogen bond (H···O). With increasing depth and pressure, the covalent bonds of hydroxyl are lengthened and the hydrogen bonds are shortened, until the two bond lengths become equal with H reaching the symmetrical center of the two adjacent oxygen atoms. The symmetrization of hydroxyl bonding was observed in $H_2O$ ice VII to ice X transition at 60 GPa and room temperature[11]. Theory further predicted that at high *T,* the $H^+$ (proton) becomes itinerant in the ice crystal lattice and moves freely like a fluid within a framework of oxygen, reaching the superionic state[12]. The challenging experiments of superionic ice have been actively pursued during the past two decades[12,13] and observed very recently with nanosecond X-ray diffraction (XRD) in laser shocked high *P-T* experiments[14,15].

Up to now the exotic superionic state has only been considered for pure $H_2O$ ice X which is an insignificant phase in the Earth's deep interior. Hydrogen in the deep Earth is mostly hidden in hydrous minerals. Here, we investigate further *P-T* effects beyond symmetrization, and report the observations of new "relaxation" and superionic states that the protons are liberated from their localized bonded states and become highly diffusive moving freely throughout the host phase. The dramatic changes of the fundamental bonding nature and mobility mandate a re-evaluation of the role of hydrogen in the deep Earth.

We initiate the research by focusing our investigation on the newly discovered Py-type $FeO_2H_x$ ($x \leq 1$)

which is a candidate hydrogen-bearing phase in the core mantle boundary (CMB)[16-19]. $FeO_2H_x$ ($x \leq 1$) has the same pyrite-type structure as $FeO_2$ but features an expanded volume due to the incorporation of H. Previous experiments exhibit a range of $x$ from 0.4 to 1.0 for $FeO_2H_x$ (Extended Data Fig. S1). Synthesized above 75 GPa, the H in Py-$FeO_2H_x$ is already in the symmetric position (Extended Data Fig. S2). Using first-principles computations and electrical conductivity, XRD and Raman spectroscopic measurements in a diamond-anvil cell (DAC) over a *P-T* range pertinent to the DLM, we observed not only the superionic state in Py-$FeO_2H_x$ above 1800 K and 121 GPa, but also a previously unknown intermediate bond-softening transition. The superionic proton conduction induces remarkable increases in the charge and mass transport that greatly impacts on the geophysical and geochemical processes in the deep lower mantle (DLM) and particularly near the CMB.

**Superionic $FeO_2H_x$ from first-principles calculation**

We study the superionic state of the Py-$FeO_2H_x$ by first-principles molecular dynamics (FPMD) calculations and predict the phase boundary of ordered crystalline and the superionic phase (Fig. 1, details in Methods). We track the motions of atoms in the Py-$FeO_2H_x$ ($x$ = 1 and 0.5) supercell at 1500-3300 K and 80-140 GPa. The length of each simulation is equivalent to 10 picoseconds. During initial heating, localized H diffusion is observed even at relatively low temperatures and the movements of protons are described by small mean-square displacement (MSD) values and low diffusion coefficients $D_H$ (Extended Data Figs. S3-S4). With further heating (e.g. 2000 K and 80 GPa), the protons start to become unbounded with a finite degree of localization, which is signified by the monotonical increment of MSD with simulation time and sudden improvement of $D_H$ (Extended Data Fig. S4). The liquid-like motion of $H^+$ in the solid $FeO_2$ lattice suggests that Py-$FeO_2H_x$ enters a superionic state

above 2000 K at 80-130 GPa. The proton diffusivity further increases with temperature and eventually, $H^+$ is delocalized from the O-H-O triplet, promoting to the so-called delocalized superionic phase with even faster proton diffusion[20]. Based on our FPMD simulation, the Py-$FeO_2H_x$ is predicted to enter the superionic state above ~1700 K from 80-130 GPa that covers even the coldest DLM geotherm (Fig. 1).

**The O-H bonding in $FeO_2H_x$**

The consequence of superionic state is multifold. Delocalized H atoms break hydroxyl bonding, a signature of hydrous minerals. Although it is technically challenging to recognize the motion of H atoms by experiment, the evolution of O-H bonding is sensitive to Raman spectroscopy. We collected the Raman spectra of Py-$FeO_2H_x$ at room temperature after it was synthesized at 2200 K and 94 GPa and decompressed to 51 GPa (Fig. 2). Below 73 GPa, the stiffening of O-H stretching mode around 3500 $cm^{-1}$ is consistent with the symmetric O-H-O bonds (Extended Data Fig. S2). However, above 73 GPa, the same mode softens precipitously, indicating the enhancement of $H^+$ mobility. The intensity of O-H Raman peak is also weakened by approximately 55%. The observations are consistent with our FPMD simulation, which shows that protons are activated and diffuse locally, thus weakening the symmetric O-H-O bonds. The restrained diffusion of $H^+$ in the Py-$FeO_2H_x$ at high-$P$, low-$T$ can be described by a relaxation state, which is regarded as a low-$T$ precursor of superionic state; high-$T$ is needed to increase the mobility beyond the unit cell level.

**Observations of superionic state by electrical conductivity measurement**

In the superionic state, the intensities of Raman signal from the O-H bonds will be greatly reduced and

no longer be an effective probe. However, electrical conductivity $\sigma$ (*EC*), which is the sum of $FeO_2$ lattice electron mobility (*EM*) and ionic conductivity (*IC*), provides the diagnostic of mobile $H^+$:

$$\sigma = \sigma_{EM} + \sigma_{IC} \quad (1)$$

The contribution of $\sigma_{IC}$ directly relates to the mobility of $H^+$, while $\sigma_{EM}$ mainly stems from electron-phonon (*e-ph*) and electron-electron (*e-e*) scattering in the $FeO_2$ lattice (see Methods). We calculated the *IC* in the predicted superionic regime by following the Nernst-Einstein equation (details in Methods). In Fig. 3**a-c**, the *IC* from proton is in the orders of $10^{2.5}$-$10^{3.0}$ S/m at ~3000 K and further boosted in the presence of electrical field[21]. While *IC* is negligible compared to *EM* at low temperature, the delocalized superionic state will significantly boost the *IC*, that will make detectable contribution to the total *EC*.

We then conducted *in-situ* 4-probe *EC* measurements on the Py-$FeO_2H_x$. The sample was initially synthesized at 113 GPa by laser heating for one hour and the *EC* experiment was performed at 121 GPa during a heating cycle up to 3300 (±200) K (see Methods for details). It is worth noting that the hydrogen content *x* and the chemical composition of the sample is well-kept before and after the *EC* experiment run, checking by high-pressure XRD (Extended Data Fig. S5 and S6). In Fig. 3**c**, a kink with $\sigma$ surging by a factor of 2 was observed around 1800-2000 K. This is well-explained by the onset of the superionic proton conduction mechanism. Here, we included the effects of induced electrical field (see Methods) and estimated the contribution of *IC* from first-principles calculations in the full temperature range. The *IC* contribution accounted for roughly one third of the total *EC* and plateaued above ~2400 K which might be due to the saturation of both *IC* and *EM* (Fig. 3**c**). This observation indicates the total *EC* of Py-$FeO_2H_x$ is of the same order as $10^4$ $S \cdot m^{-1}$, exceeding the *EC* values of all

known anhydrous lower mantle minerals, including bridgmanite (Brg)[22,23], post-perovskite (PPv)[22], and ferropericlase (Fp)[24] by at least 2 orders of magnitude at CMB conditions (Table 1). It is worth noting that the high *EC* of Py-$FeO_2H_x$ is still several orders of magnitude lower than that of metals using the same experimental scheme[25], and its positive correlation with increasing *T* is opposite to metals.

**Implications of H behaviors in Earth's interior**

The observed transitions from hydroxyl O-H to highly diffusive H in oxides lead to paradigm changes in hydrogen cycles[16] and reservoirs[26] in the DLM. First, all previous implications related to hydration in Earth's interior would be enhanced in the DLM. For instance, the long-period electromagnetic data from length-of-day series and geographical-geomagnetic measurements [C-responses[27]] combined with laboratory high *P-T EC* data of lower-mantle minerals have provided a powerful constraint on the thermo-chemical structure of the lower mantle[28]. The unusually high *EC* and the positive correlation between *T* and *EC* for superionic Py-$FeO_2H_x$ enhance the possibility of separating the thermal and hydration effects. They will eventually help to detect hydrogen and oxygen reservoirs previously proposed for the ultralow velocity zone on the basis of elasticity measurements[29]. The high *EC* and superionic mass transport might also contribute substantially to deep mantle thermal conductivity[30]. Thorough mineral physical investigations of the superionic phases would furnish a comprehensive geophysical insight into the enigmatic *D*" layer.

Moreover, superionic Py-$FeO_2H_x$ introduces a new geochemical scenario which has rarely been considered before. The Earth's interior was thought to consist of either solid minerals which were

immobile and only reached local chemical equilibrium, and fluids which were mobile and promoted equilibrium over an extended region. Superionic Py-$FeO_2H_x$ is a new type of solid consisting of fluid-like mobile $H^+$ diffusing freely in the lattice framework of oxygen and other cations. Unlike the upper mantle in which the regional geochemistry is dictated by the oxygen fugacity and redox state, the DLM geochemistry would be characteristic of the regional homogeneous hydrogen fugacity and heterogeneous redox states. The integer hydrogen stoichiometry in low-*P* hydrous minerals, such as α- and ε-$FeO_2H$, shifts to a fraction, such as the Py-$FeO_2H_x$ in the superionic region. Hydrogen fugacity may become a measurement of geochemistry in the superionic regions, where a very unusual oxygen stoichiometry[31], and distinct redox state may appear[32,33]. Superionic proton conduction introduces a mass transport mechanism, which also raises intriguing insights into the hydrogen isotope geochemistry of the deep Earth. The $\delta$D values collected from mantle-derived rocks retain many geochemical signatures of Earth's deep-water cycles. Assessment of D/H isotopic fractionation from oceanic basalts indicate that $\delta$D is generally homogeneous (with $\delta$D = -60 ± 5 ‰ compared to Standard Mean Ocean Water)[34] after removing sea water contamination. Rapid mass transport and isotope exchange by H and D diffusion could be one of the controlling factors at these depths.

The stability of $FeO_2H_x$, either partially ($x$<1) or fully hydrogenated ($x$=1), has been well established experimentally by at least four research groups[16-19,35]. Superionic $FeO_2H_x$ is a stable, minor phase along the relative cold deep subduction slabs (Fig. 1)[36]. The superionization mainly depends upon the combined *P-T* effects on the $H^+$ mobility in oxygen sublattices. It should be noted that the Py-$FeO_2H_x$ is just the first example of superionic phases in the DLM. Very likely hydrogen in the recently discovered dense hydrogen-bearing oxides that are stable under the DLM's high *P-T* conditions, such

as dense hydrous phases, may also exhibit superionic behavior. We are facing a new and refreshing view of DLM geophysics and geochemistry with answers lying in extensive mineral physics investigations of their superionicity.

**Experimental Methodology**

The multiple requirements of sample synthesis, hydrogen containment, conductivity measurements, and *in-situ* sample and hydrogen characterization under the extreme *P-T* conditions would normally present a great challenge. Fortunately, such techniques have already been well developed and perfected during the past two decades due to the similar, but more stringent experimental requirements in the quests of metallic hydrogen and room-temperature superconductors up to 400 GPa. Some very recent examples include the breakthrough of near room-temperature superconductivity of hydrogen-rich systems synthesized with or without laser-heating above 200 GPa[37,38], and semimetallic transition of hydrogen at 380 GPa[39] using the four-probe method and c-BN insulating gasket as in the present work, and x-ray crystallography of hydrogen phase III using c-BN as a low-background gasket up to 254 GPa[40]. It has been established that c-BN gasket can reliably seal bulk hydrogen with a small amount of hydrogen lost by infiltrating into the gasket. Using this matured ultrahigh-pressure technology, our present experiment at much lower pressures ~120 GPa is quite robust.

Our experiments consist of two stages. During the first synthesis stage, the solid goethite sample and four electric leads were loaded in c-BN/Re double gasket, compressed to 113 GPa, and heated to 2000 K for approximately one hour to ensure complete conversion to Py-$FeO_2H_x$. At room temperature under pressure, we scanned the sample with Raman probe but could not find any sign of the $H_2$ vibron,

presumably the liberated $H_2$ infiltrating through the c-BN gasket and being sealed by the outer Re gasket[41]. During our second stage experiment, the sample assemblage was laser-heated again with simultaneous *EC*-measurement (Fig. 3**c**). We took XRD patterns before and after the *EC* experiment (Extended Data Fig. S5 and S6), and confirmed that the sample remained stable as Py-$FeO_2H$ with $x$ fixed to the maximum stoichiometry allowed by the structure that is 0.87(8) in the present work. Details are given in the Methods section.

The maximum amount of fluid hydrogen released to form $FeO_2H_{0.86}$ is approximately 0.5-2 vol % of the solid volume. Because our Raman detection limit is 0.2% $H_2$, most $H_2$ is expected to lose through the c-BN gasket. However, combining XRD and Raman scanning, we are confident that there is no significant escape of $H_2$ in the *EC* experiment run, which means our data in Fig. 3 were reproduced under a chemically stable environment. Our experiment results suggest the surge of *EC* occurs in between 1700-1800 K and 121 GPa. At the corresponding *P-T* conditions, the *EC* of fluid $H_2$ or superionic $H_2O$ are below that of $FeO_2H_x$ (ref. 42 and Extended Data Fig. S7). Therefore, even if a small amount of $H_2$ or $H_2O$ alloyed with $FeO_2Hx$ sample, the *EC* of the sample is unlikely to be enhanced.

## References


1 Pamato, M. G. *et al.* Lower-mantle water reservoir implied by the extreme stability of a hydrous aluminosilicate. *Nature Geosci.* **8**, 75 (2014).

2 Schmandt, B., Jacobsen, S. D., Becker, T. W., Liu, Z. & Dueker, K. G. Dehydration melting at the top of the lower mantle. *Science* **344**, 1265-1268 (2014).

3 Wang, D., Mookherjee, M., Xu, Y. & Karato, S.-i. The effect of water on the electrical conductivity of olivine. *Nature* **443**, 977-980 (2006).

4 Yoshino, T. & Katsura, T. Electrical conductivity of mantle minerals: Role of water in conductivity anomalies. *Annu. Rev. Earth Planet. Sci.* **41**, 605–628 (2013).

5 Chang, Y.-Y., Hsieh, W.-P., Tan, E. & Chen, J. Hydration-reduced lattice thermal conductivity of olivine in Earth's

upper mantle. *Proc. Natl. Acad. Sci.* **114**, 4078-4081 (2017).
6 Mao, Z. *et al.* Velocity crossover between hydrous and anhydrous forsterite at high pressures. *Earth Planet. Sci. Lett.* **293**, 250-258 (2010).
7 Litasov, K. D. & Ohtani, E. in *Advances in High-Pressure Mineralogy* Vol. 421 *Geol. Soc. Amer. Spec. Paper* (ed E. Ohtani) 115-156 (Geol. Soc. Amer., 2007).
8 Hirschmann, M. M. Water, melting, and the deep Earth $H_2O$ cycle. *Annu. Rev. Earth Planet. Sci.* **34**, 629-653 (2006).
9 Jacobsen, S. D. & van der Lee, S. *Earth's deep water cycle*. Vol. 168 (American Geophysical Union, 2006).
10 Ni, H. *et al.* Distribution, cycling and impact of water in the Earth's interior. *Natl. Sci. Rev.* **4**, 879-891 (2017).
11 Goncharov, A. F., Struzhkin, V. V., Somayazulu, M., Hemley, R. J. & Mao, H. K. Compression of ice to 210 GPa: Evidence for a symmetric hydrogen bonded phase. *Science* **273**, 218-220 (1996).
12 Cavazzoni, C. *et al.* Superionic and metallic states of water and ammonia at giant planet conditions. *Science* **283**, 44-46 (1999).
13 Sugimura, E. *et al.* Experimental evidence of superionic conduction in $H_2O$ ice. *J. Chem. Phys.* **137**, 194505 (2012).
14 Millot, M. *et al.* Experimental evidence for superionic water ice using shock compression. *Nature Phys.* **14**, 297-302 (2018).
15 Millot, M. *et al.* Nanosecond X-ray diffraction of shock-compressed superionic water ice. *Nature* **569**, 251-255 (2019).
16 Hu, Q. *et al.* Dehydrogenation of goethite in Earth's deep lower mantle. *Proc. Nat. Acad. Sci. U.S.A.* **114**, 1498-1501 (2017).
17 Nishi, M., Kuwayama, Y., Tsuchiya, J. & Tsuchiya, T. The pyrite-type high-pressure form of FeOOH. *Nature* **547**, 205 (2017).
18 Boulard, E. *et al.* $CO_2$-induced destabilization of pyrite-structured $FeO_2Hx$ in the lower mantle. *Natl. Sci. Rev.* **5**, 870-877 (2018).
19 Yuan, L. *et al.* Chemical reactions between Fe and $H_2O$ up to megabar pressures and implications for water storage in the Earth's mantle and core. *Geophys. Res. Lett.* **45**, 1330-1338 (2018).
20 Hernandez, J.-A. & Caracas, R. Superionic-superionic phase transitions in body-centered cubic $H_2O$ ice. *Phys. Rev. Lett.* **117**, 135503 (2016).
21 Futera, Z., Tse, J. S. & English, N. J. Possibility of realizing superionic ice VII in external electric fields of planetary bodies. *SCi. Adv.* **6**, eaaz2915 (2020).
22 Ohta, K. *et al.* The electrical conductivity of post-perovskite in Earth's D"layer. *Science* **320**, 89-91 (2008).
23 Sinmyo, R., Pesce, G., Greenberg, E., McCammon, C. & Dubrovinsky, L. Lower mantle electrical conductivity based on measurements of Al, Fe-bearing perovskite under lower mantle conditions. *Earth Planet. Sci. Lett.* **393**, 165-172 (2014).
24 Ohta, K., Yagi, T., Hirose, K. & Ohishi, Y. Thermal conductivity of ferropericlase in the Earth's lower mantle. *Earth Planet. Sci. Lett.* **465**, 29-37 (2017).
25 Zhang, Y. *et al.* Reconciliation of experiments and theory on transport properties of iron and the geodynamo. *Phys. Rev. Lett.* **125**, 078501 (2020).
26 Mao, H.-K. *et al.* When water meets iron at Earth's core–mantle boundary. *Natl. Sci. Rev.* **4**, 870-878 (2017).
27 Khan, A. & Shankland, T. J. A geophysical perspective on mantle water content and melting: Inverting electromagnetic sounding data using laboratory-based electrical conductivity profiles. *Earth Planet. Sci. Lett.* **317-318**, 27-43 (2012).
28 Deschamps, F. & Khan, A. Electrical conductivity as a constraint on lower mantle thermo-chemical structure.

*Earth Planet. Sci. Lett.* **450**, 108-119 (2016).
29 Liu, J. *et al.* Hydrogen-bearing iron peroxide and the origin of ultralow-velocity zones. *Nature* **551**, 494 (2017).
30 Hsieh, W.-P., Deschamps, F., Okuchi, T. & Lin, J.-F. Effects of iron on the lattice thermal conductivity of Earth's deep mantle and implications for mantle dynamics. *Proc. Natl. Acad. Sci., U. S. A.* **115**, 4099–4104 (2018).
31 Liu, J. *et al.* Altered chemistry of oxygen and iron under deep Earth conditions. *Nat. Commun.* **10**, 153 (2019).
32 McCammon, C. The paradox of mantle redox. *Science* **308**, 807-808 (2005).
33 Stagno, V., Ojwang, D. O., McCammon, C. A. & Frost, D. J. The oxidation state of the mantle and the extraction of carbon from Earth's interior. *Nature* **493**, 84-88 (2013).
34 Clog, M., Auband, C., Cartigny, P. & Dosso, L. The hydrogen isotopic compositions and water content of southern Pacific MORB: A reassessment of D/H ratio of the depleted mantle reservior. *Earth Planet. Sci. Lett.* **381**, 156-165 (2013).
35 Boulard, E. *et al.* Ferrous iron under oxygen-rich conditions in the deep mantle. *Geophys. Res. Lett.* **46**, 1348-1356 (2019).
36 Yoshino, T., Baker, E. & Duffey, K. Fate of water in subducted hydrous sediments deduced from stability fields of FeOOH and AlOOH up to 20 GPa. *Phys. Earth Planet. Inter.* **294**, 106295 (2019).
37 Struzhkin, V. *et al.* Superconductivity in La and Y hydrides: Remaining questions to experiment and theory. *Matter Radiat. at Extremes* **5**, 028201 (2020).
38 Snider, E. *et al.* Room-temperature superconductivity in a carbonaceous sulfur hydride. *Nature* **586**, 373-377 (2020).
39 Eremets, M. I., Drozdov, A. P., Kong, P. P. & Wang, H. Semimetallic molecular hydrogen at pressure above 350 GPa. *Nat. Phys.* **15**, 1246-1249 (2019).
40 Ji, C. *et al.* Crystallography of low Z material at ultrahigh pressure: Case study on solid hydrogen. *Matter Radiat. at Extremes* **5**, 038401 (2020).
41 Gregoryanz, E. *et al.* Everything you always wanted to know about metallic hydrogen but were afraid to ask. *Matter Radiat. at Extremes* **5**, 038101 (2020).
42 Weir, S. T., Mitchell, A. C. & Nellis, W. J. Metallization of fluid molecular hydrogen at 140 GPa (1.4 Mbar). *Phys. Rev. Lett.* **76**, 1860-1863 (1996).
43 Ohta, K. *et al.* Electrical conductivities of pyrolitic mantle and MORB materials up to the lowermost mantle conditions. *Earth Planet. Sci. Lett.* **289**, 497-502 (2010).
44 Ohta, K. *et al.* Experimental and theoretical evidence for pressure-induced metallization in FeO with rocksalt-type structure. *Phys. Rev. Lett.* **108**, 026403 (2012).

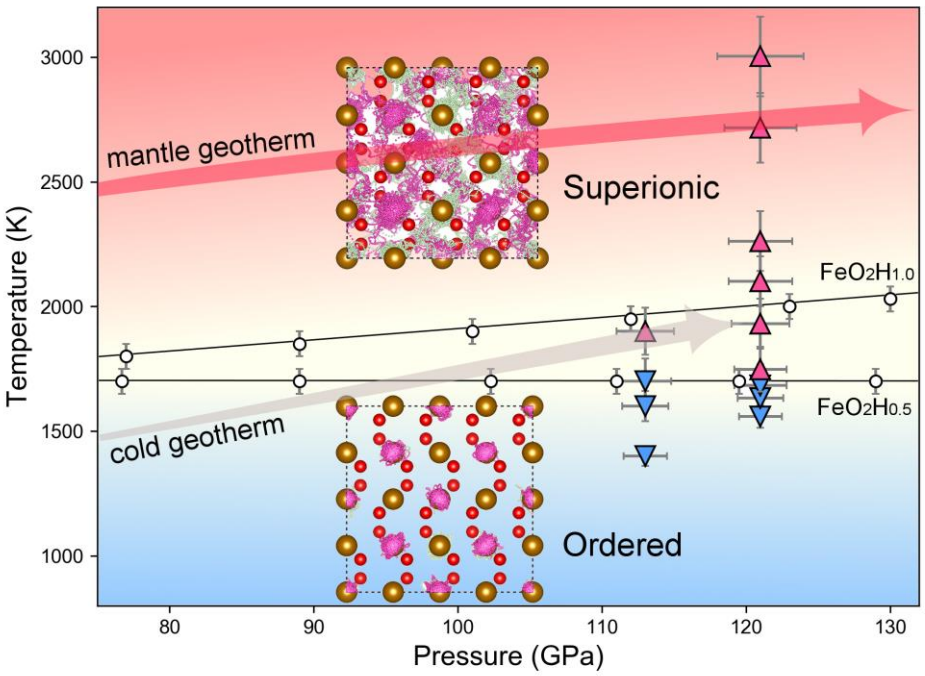


312

313 **Fig. 1. *P-T* phase diagram for ordered to superionic $FeO_2H_x$.** Open circles are data points FPMD

314 simulation. Error bars are statistic perturbation of *T* in each simulation. Uncertainty of pressure is

315 within ±2 GPa. Upward and downward triangles represent the superionic and ordered phases,

316 respectively, on the basis of *EC* measurements. Inset figures are the crystal lattice of $FeO_2$ with

317 diffusive H (purple and green clouds represent different H layers).

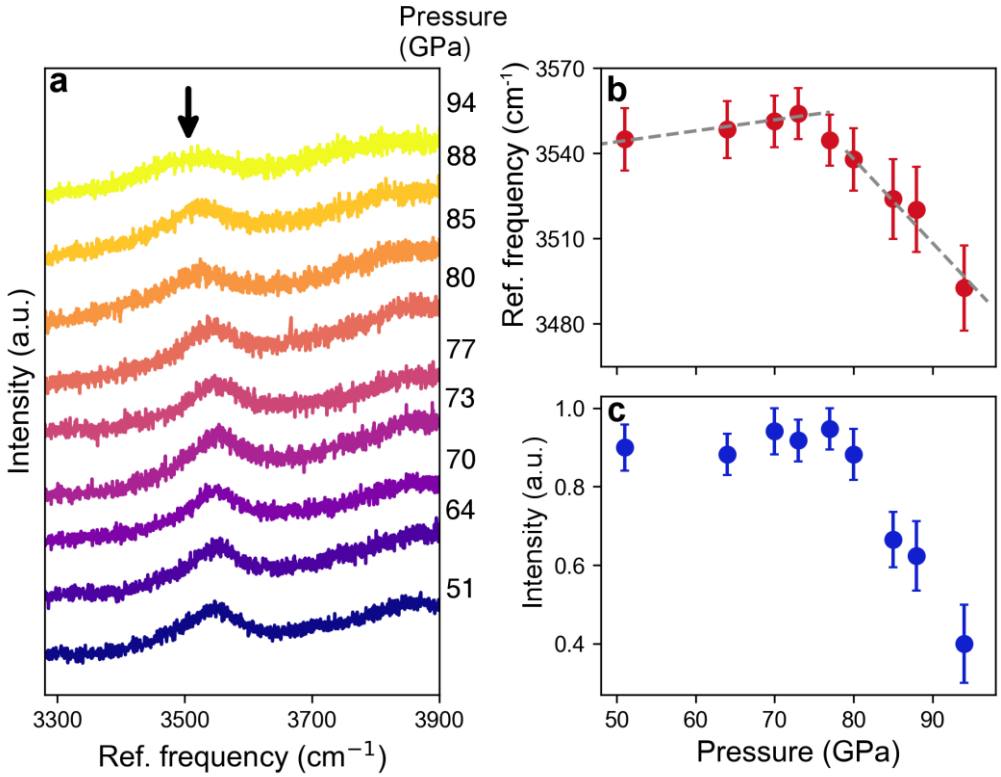


**Fig. 2. Raman spectra of a decompressed Py-$FeO_2H_x$ sample. a.** Evolution of the Raman spectrum by decompressing a Py-$FeO_2H_x$ sample from 94 GPa. The black arrow denotes the O-H Raman mode. Color gradient represent the change of pressures. **b-c.** Change of O-H mode position and intensity. The modes become softened from 77 to 94 GPa. Errors bars are derived from Gaussian-type peak fitting. The pressure media was Ar. Uncertainty of pressure is ±2 GPa.

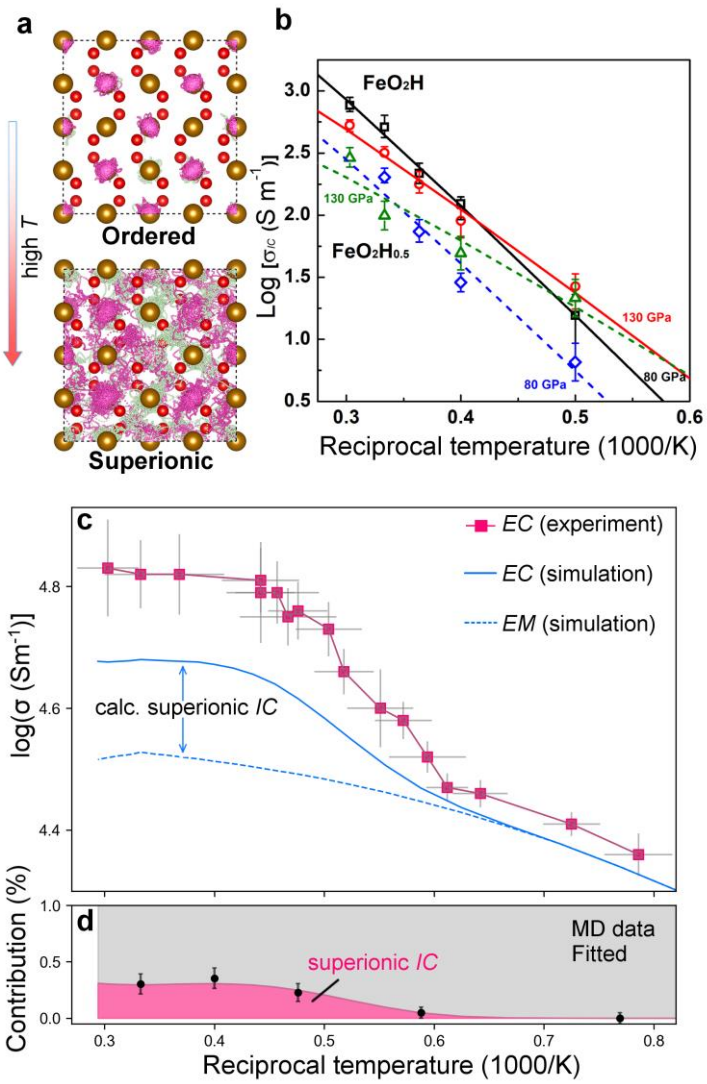


**Fig. 3. Superionic transition in Py-$FeO_2H_x$. a.** The evolution of proton trajectories of $FeO_2H_{0.5}$ from the solid to superionic state. Trajectories with different colors represent different H layers. **b.** Calculated *IC* of $FeO_2H$ and $FeO_2H_{0.5}$. Black, red, blue and green symbols represent *IC* of $FeO_2H$ at 80 GPa, $FeO_2H$ at 130 GPa, $FeO_2H_{0.5}$ at 80 GPa and $FeO_2H_{0.5}$ at 130 GPa, respectively. **c.** Total *EC* at 121 GPa upon laser heating. Experiment is compared with simulation (blue curve), which summed up values of calculated *EM* (dashed line) and *IC* under a static electrical field along the [100] direction. **d**. Theoretical calculation predicts *IC* makes approximated one third of total *EC* in the superionic state.

**Table 1. *EC* values of mantle materials.** Values were taken at various pressures and temperatures in the ascending *EC* values. The *EC* of Py-$FeO_2H_x$ is of the same order as metallic FeO at CMB conditions.

| Material | *P* (GPa) | *T* (K) | *EC* (S/m) |
|---|---|---|---|
| $(Mg_{0.9},Fe_{0.1})SiO_3$, Brg[22] | 117 | 2660 | $3\times10^{-2}$ |
| Pyrolite[43] | 129 | 2000 | $1.5\times10^{1}$ |
| $Mg_{0.83},Fe_{0.21}Al_{0.06}Si_{0.91}O_3$, Brg[23] | 82 | 2000 | $7.1\times10^{1}$ |
| $(Mg_{0.9},Fe_{0.1})SiO_3$, PPv[22] | 143 | 3000 | $1.4\times10^{2}$ |
| $(Mg_{0.81},Fe_{0.19})O$, Fp[24] | 116 | 2000 | $3.5\times10^{2}$ |
| $(Mg_{0.81},Fe_{0.19})O$, Fp[24] | 131 | 2730 | $5.5\times10^{2}$ |
| MORB[43] | 133 | 3000 | $5.6\times10^{2}$ |
| **Py-$FeO_2H_x$ (this study)** | **121** | **3000** | $\mathbf{6.6(5)\times10^{4}}$ |
| FeO wüstite[44] | 135 | 3700 | $9.0\times10^{4}$ |

## Methods

### Simulation:

**Theoretical structure optimization.** In order to calculate the electrical conductivity of $FeO_2H_x$, we first optimized the pyrite-type structure of $FeO_2H_x$ to the target pressure of 120 GP under the framework of density functional theory (DFT). Using the Vienna's Ab initio Simulation Package (VASP), the structural optimization was performed by employing the generalized gradient approximation functionals, in particular the Perdew-Burke-Ernzerhof (PBE) exchange-correlation functional[45]. We treated 8 electrons (6 in 3d and 2 in 4s) of Fe, 6 electrons (2 2s and 4 2p) of oxygen, and 1s electron of hydrogen as valence electrons explicitly. A plane-wave basis set cutoff energy of 1000 eV and *k*-point sampling of 0.06 $Å^{-1}$ were used. The geometry was optimized until the interatomic force is less than 0.01 eV/Å. The optimized structure will be further applied to first-principles molecular dynamics (FPMD) simulation, dynamical mean-field theory (DMFT) calculation, and FPMD simulation under external electric field.

**FPMD simulation**. FPMD simulations were performed using the VASP package[46] and an increased cutoff energy of 800 eV. We used the same PBE functional as was implemented for structural relaxation. A single gamma-point was adopted for *k*-points sampling in FPMD. H vacancies in Py-$FeO_2H_x$ ($x$ = 0.5) were generated by removing H atoms from a large supercell of Py-$FeO_2H$ comprising of 2×2×2 conventional unit cells. FPMD simulation becomes equilibrated after 2 picoseconds (ps) at the target *P-T* with a constant number of atoms, volume, and temperature (NVT) ensemble. Trajectories of the atomic motions were taken thereafter, with 1 fs time-step and the total time of simulation is equivalent to 10 ps. Temperature was controlled by a Nosé-Hoover thermostat[47]. This computational scheme was

tested on superionic ice, whose results are consistent with previous studies (Extended Data Fig. S7).

The velocity autocorrelation functions (VACF) *C*vv(*t*) in Extended Data Fig. S2 was calculated based on our FPMD data through the following relation[48]:

$$C_{vv}(t) = \frac{1}{3N}\sum_{\alpha=1}^{N} w_H \langle v_H(0) \cdot v_H(t) \rangle$$

where, $\langle v_H(0) \cdot v_H(t) \rangle$ denotes the averaged value of the scalar products $v_H(0) \cdot v_H(t)$ for atom velocities for ion of the $w_H$ is the weight coefficient of H ions, *t* is the time and *N* is the number of H in a supercell. The vibrational density of states are calculated as the Fourier transform of the VACF.

**Diffusion analysis.** To calculate the proton diffusion coefficient, we performed FPMD simulations using a 2 × 2 × 2 supercell for Py-$FeO_2H_x$. It is worth noting that using a larger supercell does not change the simulation results. The simulations used the canonical ensemble with a time step of 1 fs, with the simulations lasting 7 and 15 ps at temperatures from 1500 to 3500 K. This approach is suitable for evaluating the activation enthalpy of ion migration and identifying the ion transport mechanism. To study superionic transport rigorously, we calculated the diffusion coefficient for proton transport and the mean-square displacement (MSD) of the ionic positions. The diffusion coefficient is defined as:

$$D = \lim_{0\to\infty}\left[\frac{1}{2dt}\langle[\vec{r}(t)]^2\rangle\right]$$

where *d* is the dimension of the lattice on which ion hopping takes place. The MSD

$$\langle[\vec{r}(t)]^2\rangle = \frac{1}{N}\sum_{i=1}^{N}\langle[\vec{r_i}(t+t_0) - \vec{r_i}(t_0)]^2\rangle$$

is averaged over all protons, and $\vec{r_i}(t)$ is the displacement of the *i*th proton at time *t*, and *N* is the total

number of protons in the system. In practice, the value of $D$ obtained at various temperatures can be fitted with an Arrhenius equation:

$$D = Aexp\left(\frac{-\Delta H}{kT}\right),$$

where $\Delta H$ is the activation enthalpy, $A$ is a pre-exponential factor, $k$ is the Boltzmann constant, and $T$ is the temperature. The electrical conductivity was calculated using the diffusion coefficients and the Nernst-Einstein equation:

$$\sigma = \frac{fDcq^2}{kT}$$

in which $\sigma$ is the electrical conductivity, $f$ is a numerical factor approximately equal to unity, $c$ is the proton concentration, $q$ is the electrical charge of proton, $k$ is the Boltzmann constant, and $T$ is the temperature. Although this approach is a widely used approximation, it is also known to underestimates $IC$, for example by a factor 1/3 in superionic $H_2O$[49]. In superionic $FeO_2H$, the Fe ions can change their valance states during proton conduction, thus it is valuable to consider the polarization effect to predict the ionic conductivity more accurately. Therefore, our calculated $IC$ is likely to stand on the lower bound.

We also calculated the proton diffusion coefficients $D_H$ as a function of temperature (Extended Data Fig. S4). The change in proton diffusion coefficient is continuous over the $P$-$T$ region we have studied. The relation between diffusion coefficient and temperature still obey the Arrhenius relation as we mentioned above.

**Hydrogen diffusion under static electric field.** Simulation under static electric field is to explain $IC$ values in an induced ionic current with the superionic state. We would like to note that the original

403 proton diffusion rate (without electric field) still apply to the scenario in Earth's deep interior as a
404 global electrical field is unlikely to be sustained in the earth. FPMD under external electrical field was
405 conducted in CP2K[50]. We used the same Perdew-Burke-Ernzerhof functionals for the exchange-
406 correlation part of the Hamiltonian and employed the double-zeta valence (DZV) basis set optimized
407 for the Goedecker-Teter-Hutter pseudopotentials[51] to describe the wave function. The system is studied
408 in the canonical (NVT) ensemble with 0.5-fs time step and 5-ps-long productive MD simulations. A
409 cubic 2 × 2 × 2 supercell containing 128 atoms (32 Fe, 64 O and 32 H) was fixed at lattice parameter
410 $a$ = 8.719 Å, which corresponds to a pressure of 120 GPa taken from our previous MD simulation
411 without electrical field. The propagation of FPMD simulation is controlled by the optimal-sampling
412 Generalized Langevin Equation (GLE) thermostat[52] with frequency centered at 3500 $cm^{-1}$, which
413 approximates to the typical vibration frequency of ionic O-H bond in $FeO_2H_x$. Systems studied at each
414 temperature was equilibrated by 5 ps MD runs to ensure that the system is fully equilibrated prior to
415 the productive run. The homogeneous static electric field was uniformed applied along the [001]
416 direction across the supercell, within periodic boundary conditions, using the Berry phase
417 formulation[53].
418
419 The intensity value of electrical field is not straightforward to determine from experiment[54]. Previous
420 experiments on water ice established a nonlinear relation between ionic voltage and current and
421 indicated ionic current is in the μA level in ice. The intensity of the electrical field excited by proton
422 conduction can be estimated as follows,
423 $$E_{IC} = \frac{I_{IC}}{\sigma_{IC} S}$$
424 where $I_{IC}$ is the ionic current, $\sigma_{IC}$ is the electrical conductivity related to proton condition, and $S$ refers

to the lattice plane perpendicular to the direction of current in our simulation. By estimating 5~30 % of total *EC* coming from *IC*, $E_{IC}$ is derived to be in the order of 0.05~0.5 V/Å. Here, we tried intensities of 0.12, 0.26 and 0.5 V/Å as well as zero-field conditions (Fig. 2b). We found the value of 0.26 V/Å can correctly reproduce the trend of *EC* in experiment. This is also a sensitive value that have previously described the electrical properties of ice Ih, ice XI[54] and superionic $H_2O$[21].

**Calculation of electron mobility (*EM*).** The electron mobility makes an essential contribution to the total *EC*, especially at relatively low temperature. Here we computed both electron-phonon (*e*-ph) and electron-electron (*e*-*e*) contributions to the *EM* in superionic $FeO_2H_x$. We have used dedicated method for each contribution. First, we computed the *e*-ph contribution based on the FPMD simulations we previously conducted for $FeO_2H$ at ~120 GPa and various temperatures. The contribution was calculated using Kubo-Greenwood formula[55,56]. At each temperature, 30-40 FPMD simulation snapshots were selected every 0.2 ps to maintain statistically independent atomic configurations. as averages of selected configurations with a post-processing tool, kg4vasp as implemented in VASP[57]. For the electronic structure calculation, a denser *k*-points mesh of 2 × 2 × 2 was used in the Monkhorst-Pack scheme.

We computed the *e*-*e* scattering contribution to *EM* using the DFT + dynamical mean-field theory (DMFT) with continuous time quantum Monte Carlo impurity solver[58] and the Kubo-Greenwood formula with the EDMFTF code[59]. This method was successfully used to calculate the *e*-*e* contribution in high-pressure iron[60].

We sum up the separately computed *e*-ph and *e*-*e* contribution in the following formula, known as the Matthiessen's rule:

$$\frac{1}{\sigma_{EM}} = \frac{1}{\sigma_{e-\mathrm{ph}}} + \frac{1}{\sigma_{e-e}}$$

The Matthiessen's rule was used in a variety of systems including strongly correlated metals and oxides[60,61]. The *EM* contribution will be finally added to the *IC* contribution as the total *EC*.

**Experiment:**

**Sample preparation.** High-purity α-FeOOH powder samples are commercially available through Alfa Aesar (CAS 20344-49-4). The *EC* measurements were conducted in a symmetric diamond-anvil cell (DAC). The beveled culet size is 150/300 μm in diameter. The Re gasket was pre-indented to 25-30 GPa and a hole of 280 μm was drilled by laser ablation. For *EC* experiment, we packed cubic boron nitride powder in the hole to isolate the four Pt electrodes from the gasket. An α-FeOOH petite was sandwiched between two LiF layers of the thermal insulator and pressure medium.

**Synthesis of Py-$FeO_2H_x$ using laser heating.** A continuous wave ytterbium-doped fiber laser was used to heat the sample in a DAC at the Center for High Pressure Science and Technology Advanced Research (HPSTAR). The wavelength of the laser is 1070 nm.

We applied laser heating opposite to the Pt leads such that the Pt leads were heated less to avoid Pt ion diffusion into the sample. The laser beam size (as small as 30 μm in diameter) covered the whole sample area (Extended Data Fig. S8). The temperature was determined by fitting the spectrum (600-800 nm at HPCAT, HPSTAR and 700-900 nm at GSECARS[62]) with Planck radiation function using

the grey-body approximation[63]. The spectra and fitting results were reduced by t-rax software[64]. The uncertainty of the temperature measurement is around 100 K throughout the experiments. Using this setup, the sample was synthesized by heating a cold-compressed goethite sample at 113 GPa and up to 2000 K with total heating duration of approximately 1 hour. The samples were then compressed to 121 GPa and *EC* measurements were performed thereafter.

**High-*P* Raman spectroscopy.** *In situ* high-pressure Raman measurements were conducted on a customized system at HPSTAR. In a separate run, we load goethite and Ar pressure medium in a new DAC. The Py-phase was synthesized at 94 GPa and 2200 K. Raman spectrums are collected during decompression. Spectrums are taken for the back-scattering geometry using an Argon laser (633 nm and power <1mW) in the range 1000-4000 $cm^{-1}$ with a spectral resolution of 1.0 $cm^{-1}$, and the resolution of laser spot is around 10 μm. The acquiring time for each spectrum is 60 s and each collection is repeated for 10 times to eliminate the effects of fluorescence and cosmic rays. Raman spectra were fitted by using Peakfit v4.12 software to determine the positions of each Raman modes.

**The 4-probe van der Pauw method.** The initial thickness of the sample is 5.21(5) μm measured by the interferometry method. We use the EOS of goethite, ε-FeOOH and $FeO_2H_x$ to estimate the *in-situ* thickness of the sample[16,29]. The volume collapse at the phase transition is set as 12%[16]. The calculation of thickness was verified by the x-ray absorption method in a separate experiment (Extended Data Fig. S8). Here, we estimate 7% of error in thickness. Offline pressure was determined from the Raman spectrum of the diamond edge with an uncertainty up to 3 GPa[65]. A high precession source meter (Keithley-6212 DC current source and Keithley-2182A nanovoltmeter) was used to measure the

resistance of the sample. The uncertainty from the machine is less than 0.1%. Under high pressure, the sample would no longer sustain its ideally flat condition. The roughness and unevenness of the sample relate to the paired reading from four electrodes. The total error of resistance is estimated from the difference between $R_{12}$ and $R_{34}$. The *EC* was calculated according to the classic van der Pauw method based on the measured resistances[66]. For high-*T EC*, we applied continuous laser heating up to the highest temperature. Heating at each temperature typically stayed for 5 minutes and resistance values were recorded and averaged over time. Temperatures fluctuations were within ±50 K during the entire heating cycle.

**High pressure x-ray diffraction.** XRD images were taken before and after *EC* experiments to verify the sample composition. XRD patterns are generally dominated by signature diffraction peaks from the Py-phase (Extended Data Figs. S5-S6). By calculating the lattice volumes of the Py-phase, the hydrogen content $x$ stayed statistically unchanged, namely from 0.87(8) before *EC* experiment to 0.86(8) after experiment. XRD experiments were conducted at both beamlines 16ID-B (sector 16) and 13ID-D (sector 13) of the Advanced Phonon Source (APS), Argonne National Laboratory (ANL) and have reached consistent results. A highly monochromatized incident x-ray beam was used with a wavelength 0.4066 Å (16ID-B) and 0.3344 Å (13ID-D) and was focused down to a beam size of 5×8 μm and 3×4 μm respectively in the full width at half maximum.

## Data availability

The data supporting the findings of this study have been deposited at the 4TU Center for Research Data (https://doi.org/10.4121/13487643.v1). Any additional data can be requested by e-mailing the corresponding author.

## Code availability

The Vienna Ab Initio Simulation Package is a proprietary software available for purchase at https://www.vasp.at/.

## References


45 Perdew, J. P., Burke, K. & Ernzerhof, M. Generalized gradient approximation made simple. *Phys. Rev. Lett.* **77**, 3865-3868 (1996).

46 Kresse, G. & Furthmüller, J. Efficient iterative schemes for ab initio total-energy calculations using a plane-wave basis set. *Phys. Rev. B* **54**, 11169-11186 (1996).

47 Nosé, S. A unified formulation of the constant temperature molecular dynamics methods. *J. Chem. Phys.* **81**, 511-519 (1984).

48 Dickey, J. M. & Paskin, A. Computer simulation of the lattice dynamics of solids. *Phys. Rev.* **188**, 1407-1418 (1969).

49 French, M., Hamel, S. & Redmer, R. Dynamical Screening and Ionic Conductivity in Water from Ab Initio Simulations. *Phys. Rev. Lett.* **107**, 185901 (2011).

50 Hutter, J., Iannuzzi, M., Schiffmann, F. & VandeVondele, J. cp2k: atomistic simulations of condensed matter systems. *WIREs Comput. Mol. Sci.* **4**, 15-25 (2014).

51 Goedecker, S., Teter, M. & Hutter, J. Separable dual-space Gaussian pseudopotentials. *Phys. Rev. B* **54**, 1703-1710 (1996).

52 Ceriotti, M., Bussi, G. & Parrinello, M. Colored-Noise Thermostats à la Carte. *J. Chem. Theory Comput.* **6**, 1170-1180 (2010).

53 Umari, P. & Pasquarello, A. Ab initio molecular dynamics in a finite homogeneous electric field. *Phys. Rev. Lett.* **89**, 157602 (2002).

54 Cassone, G., Giaquinta, P. V., Saija, F. & Saitta, A. M. Effect of electric field orientation on the mechanical and electrical properties of water ices: An ab-initio study. *J. Phys. Chem. B* **118**, 12717-12724 (2014).

55 Pozzo, M., Davies, C., Gubbins, D. & Alfè, D. Thermal and electrical conductivity of iron at Earth's core conditions. *Nature* **485**, 355-358 (2012).

56 de Koker, N., Steinle-Neumann, G. & Vlček, V. Electrical resistivity and thermal conductivity of liquid Fe alloys at high *P* and *T*, and heat flux in Earth's core. *Proc. Nat. Acad. Sci. U.S.A.* **109**, 4070-4073 (2012).

57 Di Paola, C., Macheda, F., Laricchia, S., Weber, C. & Bonini, N. First-principles study of electronic transport and structural properties of $Cu_{12}Sb_4S_{13}$ in its high-temperature phase. *Phys. Rev. Res.* **2**, 033055 (2020).

58 Haule, K. Quantum Monte Carlo impurity solver for cluster dynamical mean-field theory and electronic structure calculations with adjustable cluster base. *Phys. Rev. B* **75**, 155113 (2007).
59 Haule, K. & Birol, T. Free energy from stationary implementation of the DFT+DMFT functional. *Phys. Rev. Lett.* **115**, 256402 (2015).
60 Xu, J. *et al.* Thermal conductivity and electrical resistivity of solid iron at Earth's core conditions from first principles. *Phys. Rev. Lett.* **121**, 096601 (2018).
61 Hausoel, A. *et al.* Local magnetic moments in iron and nickel at ambient and Earth's core conditions. *Nat. Commun.* **8**, 16062 (2017).
62 Prakapenka, V. B. *et al.* Advanced flat top laser heating system for high pressure research at GSECARS: application to the melting behavior of germanium. *High Press. Res.* **28**, 225-235 (2008).
63 Shen, G., Rivers, M. L., Wang, Y. & Sutton, S. R. Laser heated diamond cell system at the Advanced Photon Source for in situ x-ray measurements at high pressure and temperature. *Rev. Sci. Instrum.* **72**, 1273-1282 (2001).
64 Holtgrewe, N., Greenberg, E., Prescher, C., Prakapenka, V. B. & Goncharov, A. F. Advanced integrated optical spectroscopy system for diamond anvil cell studies at GSECARS. *High Press. Res.* **39**, 457-470 (2019).
65 Akahama, Y. & Kawamura, H. Pressure calibration of diamond anvil Raman gauge to 310 GPa. *J. Appl. Phys.* **100**, 043516 (2006).
66 Buehler, M. G. & Thurber, W. R. An experimental study of various cross sheet resistor test structures. *J. Electrochem. Soc.* **125**, 645-650 (1978).

## Acknowledgments

We acknowledge Xueyan Du, Nana Li, Yongsheng Zhao, Wenge Yang and Eran Greenburg for assistance in conducting laser heating and *EC* measurements; Ji Cheng and Bing Li for conducting Raman; and Y. Sun for FPMD technical support. This work is supported by the National Key Research and Development Program of China (2019YFA0708502), the National Natural Science Foundation of China (Grant no. U1530402, U1930401, 41774101 and 11774015), and the Youth Innovation Promotion Association of CAS (2020394). XRD patterns were collected at High Pressure Collaborative Access Team (16ID-B) and GeoSoilEnviroCARS (13ID-D), Advanced Photon Source (APS), Argonne National Laboratory. HPCAT operations are supported by DOE-NNSA's Office of Experimental Sciences. APS is supported by DOE-BES, under contract no. DE-AC02-06CH11357. GeoSoilEnviroCARS is supported by the National Science Foundation - Earth Sciences (EAR - 1634415) and Department of Energy - Geosciences (DE-FG02-94ER14466). M.H. is supported by

NSF Grant EAR-1847707. Y.Z. is supported by China Postdoctoral Science Foundation grant 18NZ021-0213-216308. J.C. acknowledges the support of NSF Grants EAR-1723185. C.J.P. is supported by a Royal Society Wolfson Research Merit Award. R.J.N. is supported by the Engineering and Physical Sciences Research Council under the Grant EP/P034616/1. H.K.M. is supported by NSF Grants EAR-1722515 and EAR-1447438. Q.H. is supported by a Tencent XPLORER Prize.

**Author Contributions**

Q.H, D.Y.K, and H.-K.M. formulated the concept of the study. Y.H., Q.H., B.G.J., J.H.S., D.Y.K., S. S, C.J.P. and R.J.N. conducted theoretical simulation. M.H., Y.Z. L.D., F.K., B.C., J.L. and Q.H. performed electrical conductivity measurements. Q.H. carried out the Raman. J.L., Q.H., R.T., J.C., Y.M. and V.B.P. performed XRD experiment. M.H., Y.H. and Q.H. performed the data analysis. Q.H., H.-K.M, M.H., Y.H and J.L. wrote the manuscript with contributions from all the authors.

**Competing interests**

The authors declare no competing interests.

**Correspondence and requests for materials** should be addressed to Q. Hu (qingyang.hu@hpstar.ac.cn), D. Y. Kim (duckyoung.kim@hpstar.ac.cn) and J. Liu (jin.liu@hpstar.ac.cn)